The influence of viscous slab rheology on numerical models of subduction

Natalie Hummel[1,2], Susanne Buiter[1,3], and Zoltán Erdős[3]

[1]Tectonics and Geodynamics, RWTH Aachen University, Aachen, Germany, 52062
[2]Woods Hole Oceanographic Institution, Falmouth, MA, USA, 02543
[3]Helmholtz Centre Potsdam GFZ German Research Centre for Geosciences, Wissenschaftpark, Telegrafenberg, Potsdam, Germany, 14473

Correspondence: Natalie Hummel (natalie.hummel@whoi.edu)

Abstract.

Numerical models of subduction commonly use diffusion and dislocation creep laws from laboratory deformation experiments to determine the rheology of the lithosphere. The specific implementation of these laws varies from study to study, and the impacts of this variation on model behavior have not been thoroughly explored. We run simple 2D numerical models of

5   free subduction in SULEC, with viscoplastic slabs following: 1) a diffusion creep law, 2) a dislocation creep law, and 3) both in parallel. We compare the results of these models to a model with a constant-viscosity slab to determine the relative importance of each creep mechanism in subducting lithosphere and the impact of the implementation of different lithospheric flow laws on subduction dynamics. We find that dislocation creep dominates diffusion creep throughout subducting lithosphere with moderate (5 mm) grain size in the upper mantle. However, both diffusion and dislocation creep predict very high viscosities in the

10   cold core of the slab. The resulting high slab stiffness causes the subducting plate to curl under itself at the mantle transition zone, affecting patterns in subduction velocity, slab dip, and trench migration over time. Peierls creep and localized grain size reduction likely limit the stress and viscosity in the cores of real slabs. Numerical models implementing only power-law creep and neglecting Peierls creep are likely to overestimate the stiffness of subducting lithosphere, which may impact model results in a variety of respects. Our models also demonstrate a feedback between effective slab length and subduction velocity. Ana-

15   logue and numerical models with constant-viscosity slabs lack this feedback, but still capture the qualitative patterns observed in more complex models.

1   Introduction

Several mechanisms work in parallel to accommodate deformation in Earth's oceanic lithosphere. Elastic deformation is an important mechanism when the Deborah number–the ratio of relaxation time to observation time–is high (Reiner, 1964). For

20   representative lithospheric values of viscosity ($\nu = 10^{23}$ Pas) and Young's Modulus ($E = 40$ GPa), the Maxwell relaxation time ($2\nu/E$) is about 160,000 yrs (Turcotte and Schubert, 2014). On longer time scales, strain is dominated by non-recoverable deformation via discrete macroscopic breaks (brittle failure) and via several aseismic, microscopic mechanisms, including diffusion creep, dislocation creep, and Peierls creep. Diffusion creep is the translation of individual atoms or vacancies through

mineral grains (Nabarro-Herring creep) or along grain boundaries (Cobble creep). Dislocation creep is migration of linear
25 imperfections through a crystal lattice. Diffusion and dislocation creep produce strain rates proportional to the applied stress
raised to an exponent of approximately 3.5 or 1, respectively (Hirth and Kohlstedt, 2003; Karato and Wu, 1993). Peierls
creep also takes place by the migration of dislocations, but acts as a form of low-temperature plasticity due to its high stress
dependence and weak temperature dependence, rather than following a power-law relationship with stress (Guyot and Dorn,
1967).

30 The relative importance of each deformation mechanism varies over time and space with temperature, pressure, grain size,
stress, and water content. Brittle failure is typically dominant in the upper ∼30 km (Turcotte and Schubert, 2014) of the
oceanic lithosphere, where low normal stress allows fractures to form and low temperatures prevent creep from taking place.
Dislocation creep is thought to dominate deformation in the upper mantle below the brittle ductile transition (Karato et al.,
2001; van Hunen et al., 2005). However, diffusion creep may play a role in other, deeper areas that are cold or have small grain
35 sizes (Karato and Wu, 1993; van Hunen et al., 2005). Peierls creep is likely active only in areas of very high stress (>500 MPa),
such as the cold cores of subducting lithosphere (Kameyama et al., 1999), where other creep mechanisms predict very strong
behavior.

Numerical modelers have approximated the rheological properties of subducting lithosphere in a variety of ways. The sim-
plest approach is to implement constant-viscosity slabs with 2 or 3 orders of magnitude contrast with the surrounding astheno-
40 sphere (Capitanio et al., 2008; Heuret, 2007; Kaus and Becker, 2008; Quinquis et al., 2011; Schmeling et al., 2008). This
elegantly allows first-order behaviour of subducted slabs to be investigated. More commonly, the rheology of a subducting slab
is set to mimic the extrapolated behavior predicted by laboratory deformation experiments on single minerals, monomineralic
aggregates, or mantle rock types. These laboratory experiments (Chopra and Paterson, 1981; Kirby, 1983; Wilks and Carter,
1990; Karato and Wu, 1993; Hirth and Kohlstedt, 2003) quantify the stress-strain relationships of individual creep mechanisms
45 and their dependence on relevant factors such as temperature, pressure, grain size and water content. Numerical modelers have
taken various approaches to implementing the resulting flow laws. For example, Tagawa et al. (2007) model the lithosphere
using Newtonian, temperature-dependant (diffusion) creep based on data from Karato and Wu (1993), with the pre-exponential
factor adjusted to produce an average viscosity of $5 * 10^{20}$ Pas in the upper mantle, and Erdős et al. (2021) use a wet olivine
dislocation creep law from Karato and Wu (1993). Quinquis and Buiter (2014) take a slightly more complex approach fol-
50 lowing van den Berg et al. (1993), using laws determined by Hirth and Kohlstedt (2003) on wet olivine aggregates to model
diffusion and dislocation creep in parallel, such that the strain rates predicted by each mechanism are added to achieve the total
strain rate. Arcay (2012) models oceanic lithosphere with an even more complex rheological structure, including regions of
dry granulite (Wilks and Carter, 1990), wet dunite (Chopra and Paterson, 1981), dry diabase (Kirby, 1983), and wet olivine
(Karato et al., 2001; Hirth and Kohlstedt, 2003).

55 Using values from laboratory flow laws, which are extrapolated from laboratory time and spatial scales to subduction scales,
generally leads to high viscosity values in the interior of cold subducted slabs. Independent of the question of whether such high
viscosity values occur in nature, many modeling softwares cannot effectively handle the resulting large variations in viscosity.
For this reason, models generally use a maximum stress or viscosity cap. The latter varies from 10^{23} Pas (Billen et al., 2003;

Behr et al., 2022), 10^{24} Pas (Torii and Yoshioka, 2007; Quinquis and Buiter, 2014; Biemiller et al., 2019), 10^{25} Pas (Gerya
60 et al., 2021; Tagawa et al., 2007), to 10^{26} Pas (Tetreault and Buiter, 2012; Khabbaz Ghazian and Buiter, 2013). Alternatively,
modelers may impose a maximum stress on the order of 500 MPa, which roughly approximates the effect of Peierls creep
(Ĉížkovă et al., 2002; Behr et al., 2022). Though both approaches limit the strength of the lithosphere, they do not generally
produce the same slab behavior (Billen, 2008).

The stiffness of subducting lithosphere—a function of the plate thickness and viscosity contrast with the surrounding man-
65 tle—affects slab geometry, dip (Billen and Hirth, 2007; Capitanio et al., 2008), subduction velocity (Ĉížkovă et al., 2002;
Arcay, 2012), and trench motion (DiGiuseppe et al., 2008). The general mechanics and geometry of subduction have been
investigated through numerous analogue and numerical experiments. Funiciello et al. (2008) document 4 stages in analogue
models of free subduction: (1) subduction initiates and (2) the slab tip sinks through the upper mantle with increasing velocity
until (3) subduction slows temporarily as the slab interacts with the bottom of the tank, and (4) eventually reaches a steady-
70 state, with the end of the slab lying flat on the bottom of the tank and trench retreat proceeding at a constant velocity. The
numerical models of Kaus and Becker (2008), which, like the models of Funiciello et al. (2008), are driven only by buoyancy
of the subducting plate and have no overriding plate, illustrate the effect of slab stiffness on this subduction process. A sub-
ducting plate of low constant viscosity (10^{21} - 10^{22} Pas) bends at the trench and unbends to subduct forward at a steep angle
into the upper mantle, as observed by Funiciello et al. (2008). A high viscosity plate however (10^{23} - 10^{24} Pas) is too stiff to
75 unbend and keeps a side-ways U-shape or curl. In such cases, slab pull is too low for the high stiffness of the slab to achieve
slab unbending (Goes et al., 2017; Stegman et al., 2010). Increasing the slab-mantle viscosity contrast from 10^2 to 10^3 has
also been shown to decrease slab dip and increase subduction velocity in the steady-state stage of subduction (Capitanio et al.,
2008).

It is clearly important to understand how the choice of flow law in a numerical model affects slab rheology and, by extension,
80 subduction dynamics. In this study, we use simplified models of subduction to investigate the effect that creep laws (linear
viscous, diffusion, dislocation or diffusion and dislocation in parallel) have on slab viscosity, slab shape, and subduction
velocity. We quantify slab pull and the rate of internal dissipation of energy over the course of each experiment to explain
differences in subduction style between models. We hope that these experiments raise awareness of the limitations of using
extrapolated flow laws in numerical models of subduction and initiate a discussion on high viscosity values reached in many
85 models.

2 Model Set Up

In order to investigate the effects of different flow laws on slab rheology and behavior, we use 2D models of free subduction
with variable flow laws active in the slab. The models are highly simplified—self-consistent with linear viscous crust and
mantle—in order to focus on the effects of slab rheology. We implement individual flow laws to illustrate the contribution
90 of each law to deformation in the slab and investigate whether increasing rheological complexity in the slab has significant
implications for model behavior.
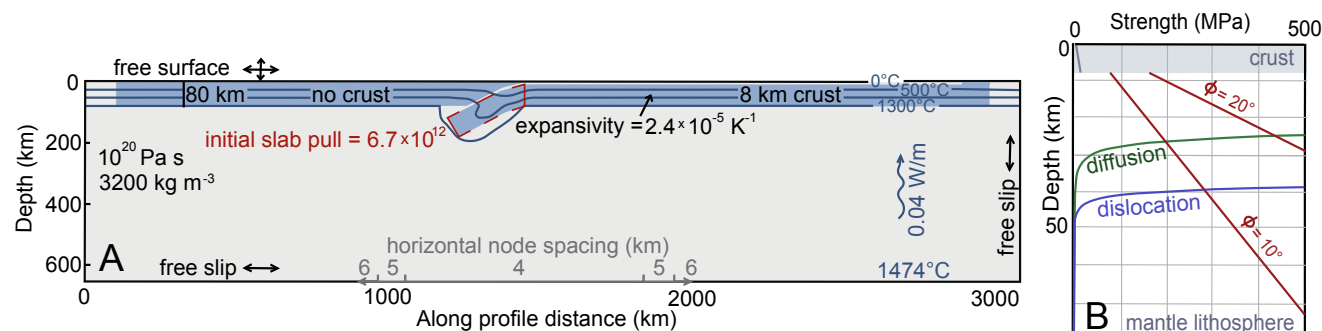
Figure 1. The initial set-up for all models. A shows the oceanic lithosphere in blue and the asthenosphere in grey, with thermal parameters in dark blue text and kinematic parameters and material properties in black text. The red box illustrates the area over which the slab density contrast compared to a background asthenospheric density profile is integrated to obtain the slab pull force. B shows strength vs depth in the lithosphere for each flow law implemented in this study, assuming a strain rate of 10^{-15} s^{-1}. Brittle failure envelopes for $\phi= 20°$ and $\phi= 10°$ are plotted in red, and diffusion and dislocation strength in green and blue.

We run experiments in SULEC, an Arbitrary Lagrangian Eulerian finite element code (Buiter and Ellis, 2012) using the PARDISO solver (Schenk and Gartner, 2004). SULEC solves conservation of energy and momentum equations for an incompressible fluid and advects tracers recording material properties through an element mesh of prescribed density. We use Courant
95   time stepping with a Courant number of 0.1 and apply a weak diffusive erosion process with a diffusion coefficient of 10^{-6} m^2s^{-1} (Culling, 1960) to limit surface instabilities.

The initial model geometry and temperature field are identical in all models (Fig. 1). The models are 3080 km wide by 660 km deep and have nodes spaced every 6 km in the x-direction, with a finer spacing around the trench (Fig. 1). The y-direction node spacing increases from 2 km at the surface to 6 km below 240 km depth. The elements have 4 nodes for velocity and
100   are constant in pressure. The subducting lithosphere is 80 km thick and 1430 km long from trench to trailing end, with an 8 km-thick crust (Fig. 1). The models have a free surface and the sides and bottom of the models are free slip. No material enters or exits the model domain. We do not impose a pushing force on the plate. Instead, subduction is driven by the density contrast between the lithosphere and the asthenosphere. In the initial set-up, a small section of the slab tip dips under the overriding plate at an angle of 30° to a depth of 183 km to facilitate subduction initiation. The subducting plate lacks crust
105   along a 100 km-long section of its trailing end, and subduction stalls when this section reaches the trench, marking the end of the experiment. We leave 100 km of asthenosphere on either side of the lithosphere to allow the plates to slide horizontally. The initial temperature field in the slab tip follows the analytical model from Davies (1999) for a subduction velocity of 12 mm/yr, but the temperature field quickly adjusts as the experiment progresses.

The rheological properties of the slab are varied to reproduce behavior that is: A–linear viscoplastic, B-viscoplastic following
110   a wet olivine diffusion creep law from Hirth and Kohlstedt (2003), C–viscoplastic following a wet olivine dislocation flow law

Table 1. Parameters for diffusion and dislocation flow laws from experiments on wet olivine aggregates (Hirth and Kohlstedt, 2003). The value of A reported here has been scaled (Ranalli) to relate the second invariants of stress and strain rate tensors, as used in SULEC, rather than relating uniaxial stress to strain rate, as recorded in the original experiments.

Parameter	Symbol	Diffusion creep	Dislocation creep
Pre-exponential factor	A	$1.5 * 10^{-18}$	$5.33 * 10^{-19}$
Power law exponent	n	1	3.5
Grain size	d (m)	0.005	–
Grain size exponent	p	3	0
Activation Energy	E^* (kJ/mol)	335	480
Activation volume	V^* (m^3/mol)	$4 * 10^{-6}$	$11 * 10^{-6}$

(Hirth and Kohlstedt, 2003), and D–viscoplastic with diffusion and dislocation creep implemented in parallel. Strength (half the differential stress) predicted by the diffusion and dislocation flow laws is plotted against depth in Figure 5B, assuming the initial $16.25°\mathrm{Ckm^{-1}}$ temperature gradient, lithostatic pressure, and a strain rate of 10^{-15} s^{-1}. To implement two laws in parallel, the strain rates predicted by each law are added. The strengths of the laws can vary by several orders of magnitude, so one law typically dominates deformation at a time. The angle of internal friction is 20° in undeformed mantle lithosphere, and weakens linearly to 10° between strains of 0.5 and 1.5. The cohesion is 20 MPa. The plastic and viscous laws are active one at a time, such that only the weaker law controls the effective viscosity of the slab.

The diffusion and dislocation flow laws follow the form:

$$\dot{\epsilon} = A\sigma^n d^p e^{\frac{-E^* + PV^*}{RT}}, \tag{1}$$

where A is an empirically determined coefficient, σ is the stress, n is the stress exponent, d is the grain size, p is the grain size exponent, E^* is the activation energy, V^* is the activation volume, P is the pressure, T is the temperature, and R is the gas constant. The values of these parameters are shown in Table 1.

The temperatures at the top and bottom boundaries of all models are fixed at 0°C and 1474°C, respectively. This imposes a nearly-constant upwards heat flux of 0.04 Wm^{-1}. In the lithosphere, which has a thermal conductivity of 2.5 Wm^{-1}K^{-1}, a thermal gradient of 16.25° per km is required to maintain this heat flux. The asthenosphere has a thermal gradient of 0.3° per km and an artificially high thermal conductivity of 135.4 Wm^{-1}K^{-1}, in order to mimic the thermal profile of a vigorously convecting mantle, which is not explicitly simulated. Elevated asthenospheric thermal conductivity is often used in numerical models of subduction (Pysklywec and Beaumont, 2004; Khabbaz Ghazian and Buiter, 2013; Erdős et al., 2021) to maintain a realistic adiabat and a constant heat flux between the asthenosphere and the overlying lithosphere without requiring time to establish vigorous convection prior to simulating processes of interest. For simplicity, we do not implement shear heating or radioactive heat production.

Table 2. Parameters used for each material in all experiments.

Parameter	Crust	Lithospheric mantle	Asthenosphere
Thickness (km)	8	80	590
Thermal expansion coefficient (K^{-1})	$2.4 * 10^{-5}$	$2.4 * 10^{-5}$	0
Density at T_0 (kgm^{-3})	3200	3200	3200
T_0 (C)	1474	1474	1474
Thermal conductivity (Wm^{-1}K^{-1})	2.5	2.5	135.42
Heat capacity (JK^{-1})	750	750	750
Viscosity (Pas)	10^{20}	variable (10^{20}-10^{26})	10^{20}

All models simulate a linear viscous asthenosphere, with a viscosity of 10^{20} Pas and a constant density of 3200 kgm^{-3} (Fig. 1). The crust on the subducting slab has a constant-viscosity of 10^{20} Pas. The overriding plate has no crust. The properties of the asthenosphere and thermal properties of the lithosphere remain constant throughout all models (Table 2). The lithospheric density is equal to that of the asthenosphere at a temperature of 1474°C ($\rho_0 = 3200$ kg/m^{-3}), and increases as temperature decreases according to:

$$\rho(T) = \rho_0 + \alpha * (T_0 - T), \tag{2}$$

where α is the coefficient of thermal expansion, $2.4 * 10^{-5}$ K^{-1}.

This produces an average density contrast of 63.3 kgm^{-3} between the asthenosphere and the un-subducted portions of the slab. We do not implement any mineral phase changes.

We simulate only the upper mantle, down to 660 km depth. The bottom of the model is a proxy for the mantle transition zone, where a viscosity increase of one or two orders of magnitude often hinders the sinking of subducting slabs (Hager, 1984). The true mantle transition zone is not impenetrable, making the free-slip model bottom an imperfect approximation (Billen, 2008). The benefit to limiting the model domain rather than simulating a viscosity increase and a lower mantle is that these models are relatively computationally cheap.

3 Results

3.1 Subduction dynamics

The subduction of the constant 10^{23} Pas viscosity slab is illustrated in Fig. 2 A and in the top row of Figure 3. The slab sinks with an increasing velocity until it makes contact with the bottom of the model —a proxy for the viscosity increase at the mantle transition zone. The slab then unbends and flattens out along the bottom of the model, reaching an approximately constant subduction velocity around 11 cm/yr (Fig. 4 A). Subduction stops when the trailing end of the subducting lithosphere, which has no crust, reaches the trench and stalls subduction by removing weak material from the interface.
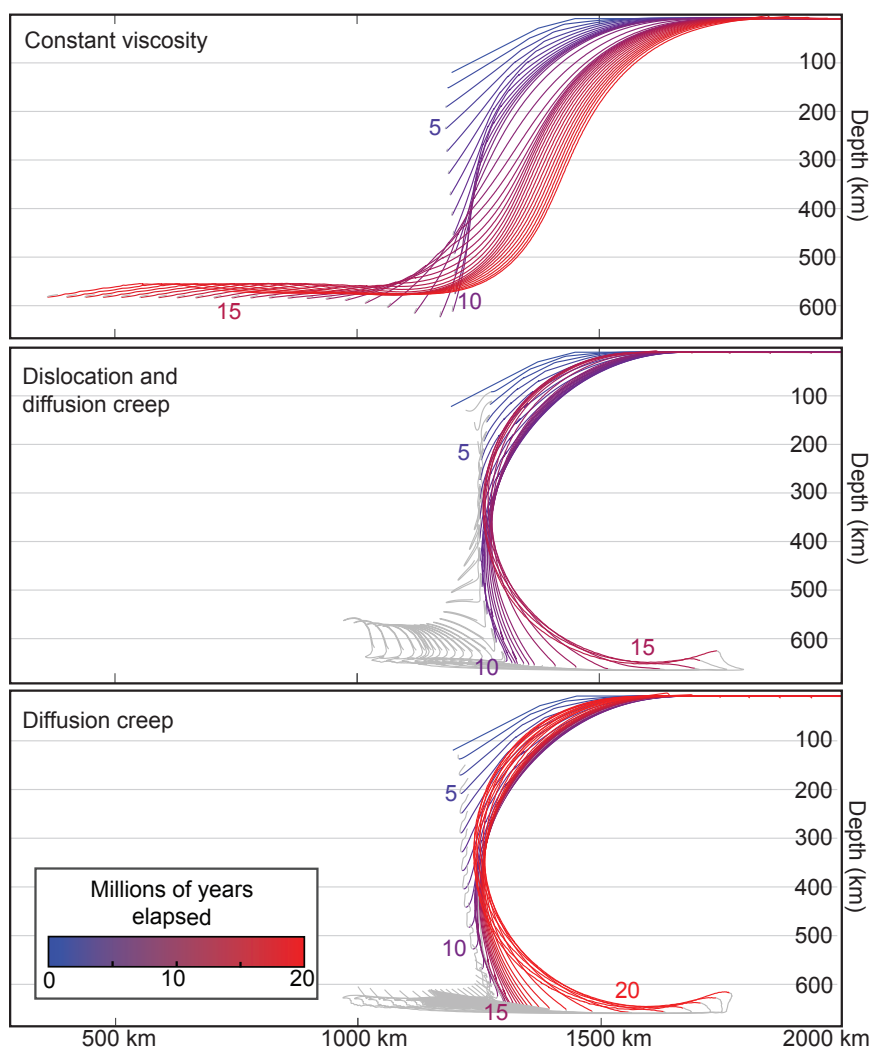
Figure 2. Lines show the interface between the crust and the mantle lithosphere in the subducting slab, colored by time from blue to red. Lines are plotted every 200 time steps. Numbers indicating elapsed time in millions of years are located next to the tips of lines at 5 million year intervals. The top plot shows results from the reference model with a constant-viscosity slab. The middle plot shows the model with dislocation and diffusion creep implemented in parallel, which is almost indistinguishable from the model with only dislocation creep (not shown). The lowest plot shows the model following only a diffusion creep law. Gray lines trace portions of the slab that have reached asthenospheric viscosity (10^{20} Pas).
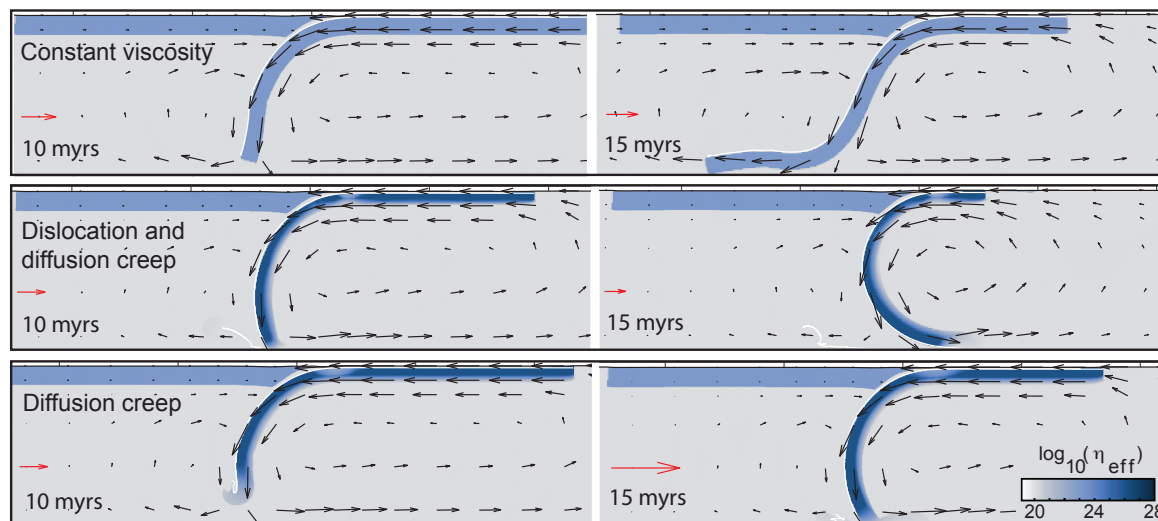
Figure 3. Slabs at 10 and 15 million years, colored by viscosity, with vectors showing the velocity field. White lines indicate material at the crust-mantle interface in the subducting plate. The plots for dislocation-only and dislocation-diffusion models are indistinguishable, so we only show results from the dislocation-diffusion model. The velocity arrows have different scales in each panel because the maximum velocity varies between the snapshots presented. Each red arrow is scaled to 10 cm/yr for the given panel. Plots use the oslo colormap from Crameri (2018).

The behavior of the three creep-governed models contrasts considerably with the behavior of the constant-viscosity model. All three models undergo a similar evolution, illustrated in Figure 2, in which the slab sinks, collides nearly orthogonally

155 with the bottom of the model, and gradually curls under itself. All three slabs sink with an increasing velocity, then slow as they near the bottom of the model (Fig. 4). Subduction then proceeds more slowly as the slabs curl under. Once the slabs have curled sufficiently—making an angle of 50° to 60° to the bottom of the model—subduction velocities increase rapidly. Subduction velocities in all three creep-governed models surpass 20 cm/yr and show no indication of stabilization before the crustless trailing end of the slab jams the trench. Convection at these later stages is concentrated below the slab, in contrast to

160 the evenly-distributed convection in the reference model (Fig. 3).

The shaded regions in Figure 4 represent the rate of trench rollback/advance over time. In all models, subduction takes place via trench rollback and advance of the un-subducted plate as the tips of the slabs fall freely through the asthenosphere. Trench rollback plays a proportionally smaller roll as subduction velocity increases. The constant-viscosity slab remains in trench retreat throughout the experiment, but the creep-governed slabs switch to trench advance as they approach the mantle

165 transition zone.
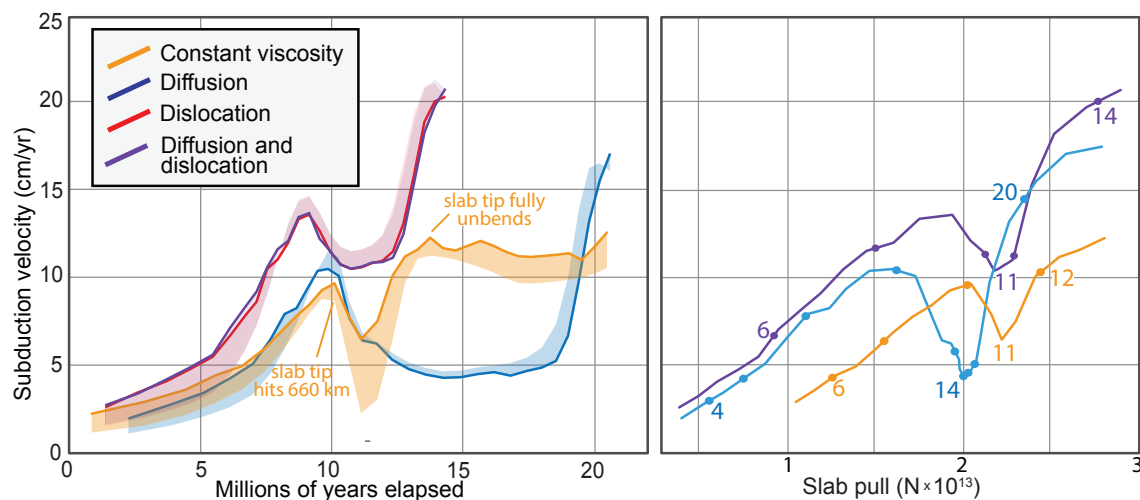
Figure 4. The plot on the left shows subduction velocity over time for each of the four models. The bold curves show the rate at which material is consumed at the trench and the opposite edge of the shaded region around each curve shows the rate of motion of the slab with respect to the model boundaries. The thickness of the shaded region therefore represents the velocity of the trench. During periods where the shaded region lies below the bold line, the model undergoes slab rollback. Where the shaded region lies above the line, there is trench advance. The plot on the right shows how subduction velocity varies with slab pull in the constant-viscosity, diffusion, and diffusion-dislocation models. The lines follow the progression of each model through time with points at 2 million year intervals. Data are only plotted until the slab begins to lie flat on the bottom of the model. Beyond this point, slab pull is no longer proportional to the density anomaly of the subducted slab, and the calculation of slab pull is less straightforward.

3.2 Slab viscosity structure

The cores of all three creep-governed slabs exceed the viscosity of the constant 10^{23} Pas reference model by several orders of magnitude. The diffusion-only slab has the highest viscosity overall. At the surface of the model, in areas with no active plastic deformation, the slab reaches the viscosity cap of 10^{26} Pas in the top 40 km (Fig. 5 Profile C). The viscosity decreases

170 between 40 and 75 km depth according to the diffusion creep law, and hits the viscosity minimum of 10^{20} Pas below 75 km. The viscosity structures of the dislocation-only and dislocation-diffusion slabs are extremely similar, suggesting that dislocation creep dominates in the upper mantle when diffusion and dislocation creep are implemented in parallel. The viscosity of the un-subducted portions of slabs with dislocation creep decreases from 10^{26} to 10^{20} Pas in the 35 to 60 km depth range. Once subducting lithosphere has heated to near-asthenospheric temperatures, its viscosity decreases to the minimum value (10^{20}

175 Pas) and its density approaches asthenospheric density. A growing proportion of the slab tip, represented by the thin gray lines in the lower two plots in Figure 2, therefore assimilates into the mantle as the model progresses.

Figure 5 shows the strength of the dislocation-diffusion slab along two profiles: one in the subducted portion of the slab around 400 km depth and one where the slab bends just before entering the trench. The true strengths—computed as half the modeled differential stress—are compared with the strength envelopes calculated analytically assuming dislocation creep,

180 diffusion creep, and brittle failure under the temperatures, pressures, and strain rates along the profiles. The true strength is controlled by the dislocation creep mechanism in regions of both profiles. In A, the true strength curve deviates from the dislocation creep curve in the top $30 \, \mathrm{km}$ of the slab where the viscosity reaches the $10^{26} \, \mathrm{Pas}$ stress cap. The slab has a constant viscosity over this interval, but lower strain rates in the middle of the slab result in lower stresses and a dip in strength centered approximately $18 \, \mathrm{km}$ into the slab. In profile B, deformation is accommodated by brittle failure in the top 20 km.

185 ### 3.3 Trench motion

The reference model undergoes trench rollback throughout the run, whereas the creep-governed models switch to trench advance after the slabs make contact with the boundary representing the 660 discontinuity. This difference is a consequence of the closed "fish tank" form of our models. After the slabs make contact with the bottom of the model, the lithosphere prevents asthenosphere from flowing between the left and right sides of the model. This causes trench rollback velocity to be linked 190 to subduction velocity, as pointed out by Billen (2008). In the constant-viscosity model, the trench moves rightward to compensate for the leftward motion of the lithosphere. In each creep-governed model, as the slab curls under itself, the rightward motion of the slab tip is balanced by trench advance to avoid compression of the material on the right side of the model. The thickness of the lithosphere is approximately one eighth of the model thickness, so the observed trench rollback/advance speeds are a comparable percentage of the subduction velocity.

195 ## 4 Force Balance and Energy Dissipation

Subduction is driven by the gravitational force on the dense lithospheric material at the surface of the model. This "slab pull" force is approximated as:

$$F_{sp} = g \int_{V slab} (\rho_{lith} - \rho_{asth}) dV, \tag{3}$$

where ρ_{lith} is the temperature dependent density of the lithosphere, g is the gravitational acceleration, and ρ_{asth} is a constant: 200 $3200 \, kg/m^3$. The density contrast is integrated over all lithospheric material that has passed through the trench into the subduction zone. Slab pull evolves as subduction progresses according to the amount and temperature of the subducted lithosphere, which are functions of subduction velocity. Subduction velocity is in turn determined by the balance between slab pull and resisting forces in the lithosphere and asthenophere.

Figure 4B shows the relationship between slab pull and subduction velocity over time in each model. The dislocation-205 diffusion and dislocation-only slabs follow very similar paths, so the data for the dislocation-only slab are not shown. At a given slab pull, the dislocation-governed slabs have a higher subduction velocity than the diffusion-governed slab, which has a higher subduction velocity than the constant-viscosity slab (Fig. 4B). This implies that the constant-viscosity model experiences the highest cumulative resisting force at a given subduction velocity.
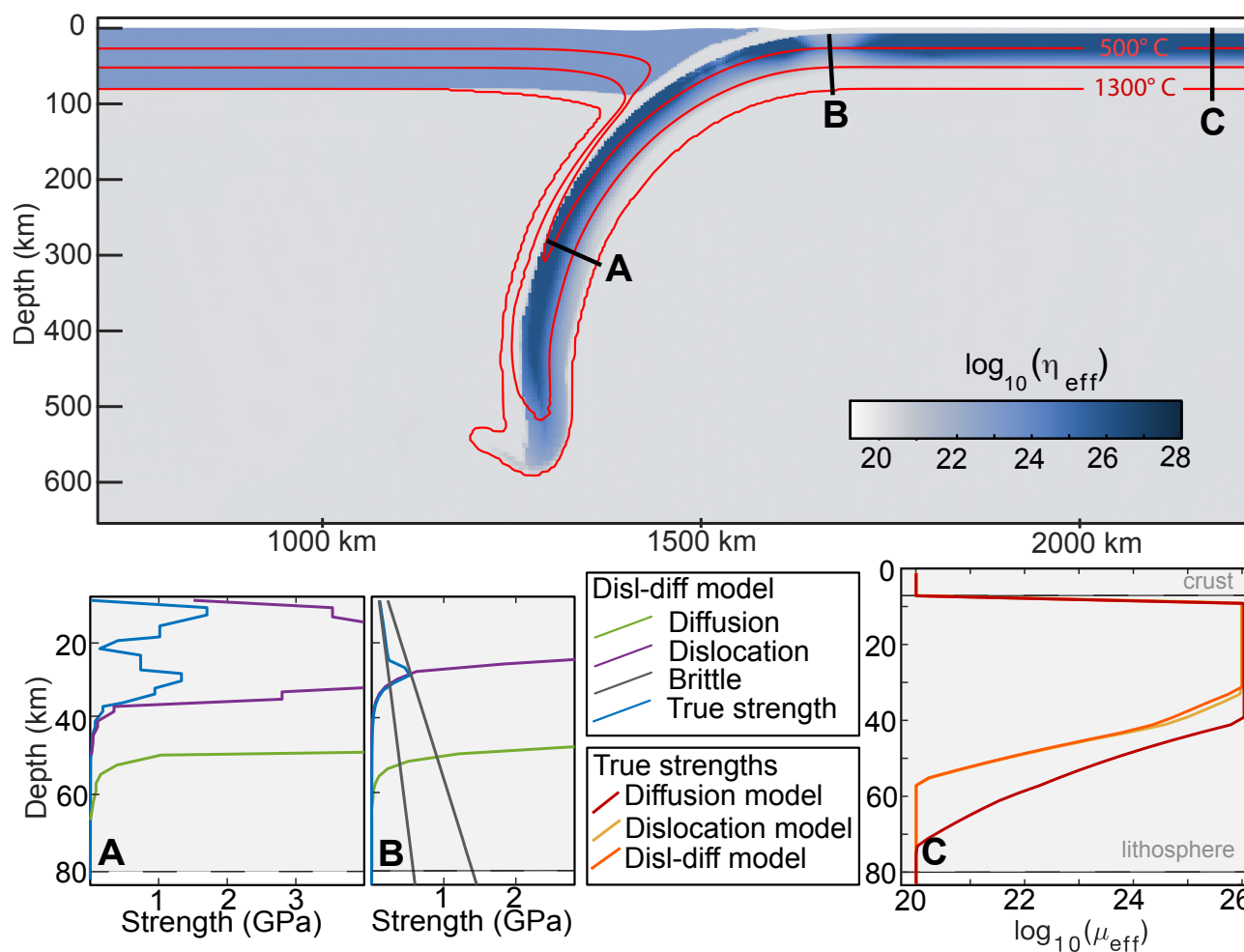
Figure 5. An image of the viscosity structure of a slab following dislocation and diffusion creep laws in parallel after 10 million years. Plots along profiles A and B show the strength of the slab (blue), compared to the strengths predicted by dislocation creep (purple), diffusion creep (green), and brittle failure (gray) with $\phi = 20°$ and $\phi = 10°$ under local strain rates and pressures. Profile A shows strength at middle depths of the upper mantle, where the upper half of the slab hits the viscosity cap and no brittle deformation is active. Plot B shows strength at the surface near the trench where the slab bends and undergoes brittle deformation. Plots in C show viscosity vs depth in the diffusion, dislocation, and diffusion-dislocation slabs. These plots represent un-subducted lithosphere with strain rates too low for plastic deformation. The location of these profiles is indicated on the model image.

We use the rate of internal dissipation of energy to compare the resistance in the crust, asthenosphere, and subducting

210   lithosphere between models (Fig. 6). The rate of internal dissipation of energy is calculated as:

$$\dot{W} = \int\limits_{V} \sigma_{\mathrm{II}} \dot{\epsilon}_{\mathrm{II}} dV, \tag{4}$$

where σ_{II} and $\dot{\epsilon}_{\mathrm{II}}$ are the second invariants of the stress and strain tensors, respectively, at a particular point in the model. Their

product is integrated over the volume of interest (e.g. the crust). This quantity is a rate of work, proportional to the forces and

the velocities throughout the volume.

215   Figure 6 shows a clear correlation between the total rate of energy dissipation and the subduction velocity in the constant-

viscosity model. This correlation applies to the other models as well (Fig. 7). Though subduction velocity does not appear in

the equation for energy dissipation rate directly, subduction drives the motion of material and therefore the rate of subduction

has a strong effect on local velocities and strain-rates. Comparing models at a given subduction velocity therefore helps to

isolate the effect of resisting force on dissipation rate.

220   From the start of each experiment until the slabs reach 660 km depth, the rate of energy dissipation in the crust of each model

is nearly identical at a given subduction velocity (Fig. 7). The rate of energy dissipation in the asthenosphere and lithosphere

are highest—by a relatively small margin—in the reference model and lowest in the models implementing dislocation creep,

resulting in a lower initial subduction velocity in the reference model. After the slabs have reached the bottom boundaries,

there is not a systematic difference in the rate of crustal or asthenospheric energy dissipation between models. However, at

225   later stages, the rate of dissipation in the lithospheric mantle is higher in the constant-viscosity slab than in the creep-governed

slabs. Therefore, the lower maximum subduction velocity in the reference model is primarily due to greater resistance in the

lithospheric mantle, relating to the length and shape of the slab.

The rate of energy dissipation in an area is proportional to local strain rate and stress. Stress in the linear viscous crust and

asthenosphere is again proportional to strain rate. Therefore, strain rate (and by extension subduction velocity) enters into the

230   equation for dissipation rate twice: once directly and once in the stress term, resulting in a generally quadratic relationship

between velocity and dissipation rate in the linear viscous materials (Fig. 7).

This relationship is complicated by the geometry of the model. For instance, the crust deforms not only along the interface

between the subducting and overriding plates, but also along a constantly increasing length of subducted lithosphere. Dissipa-

tion rate in the crust has a similar relationship to subduction velocity in all models until the tip of the slab begins to interact

235   with the bottom of the model domain around 9-10 myrs (Fig. 7). When the slab curls under after 17 myrs in the dislocation-

governed models and 11 myrs in the diffusion-governed model, dissipation rate in the crust increases dramatically compared

to the earlier stages of subduction, due in part to high dissipation in the crust dragged between the plate and the bottom of the

model (Fig. 7H). In contrast, this effect is not present in the constant viscosity model where the slab does not curl under and

the crust never gets that close to the model boundary.

240   Dissipation in the asthenosphere shows a similar dependence on subduction velocity across all models (Fig. 7), even though

convection is concentrated underneath the subducting plate in the creep-governed models and evenly distributed in the constant-

viscosity slab model (Fig. 3). It is important to note that the rheology of the asthenosphere is highly simplified, and the
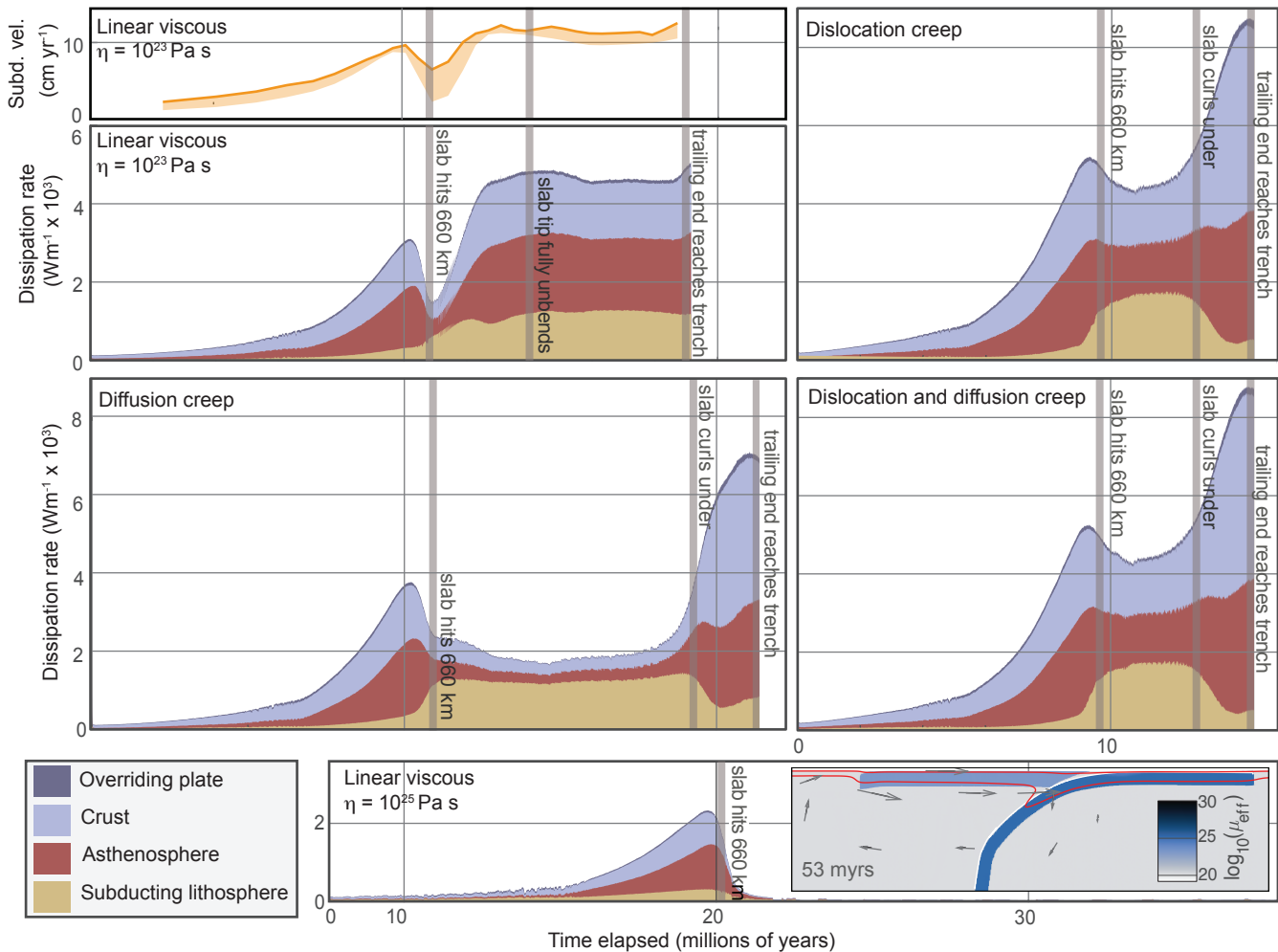
Figure 6. Dissipation of energy over time in each model. Each curve is broken down into dissipation in the crust, mantle lithosphere, asthenosphere, and the overriding plate. The lower-most plot shows results of a supplementary model, with an inset showing the slab after 53 million years of elapsed time. At this time step, subduction has slowed nearly to a stop; the largest velocity arrow represents motion at 0.5 mm/yr. The plot on the upper left shows subduction velocity for the reference model to illustrate the correlation with the total rate of energy dissipation shown in the plot below. Vertical grey bars mark notable points in the evolution of each experiment.

relationship between subduction velocity and asthenospheric dissipation rate may not remain similar between models if a more realistic rheology were implemented.

245   Once plates have made contact with the bottoms of their respective model domains, subduction velocity varies dramatically between models. Most of this difference can be attributed to patterns of energy dissipation in the mantle lithosphere 6. Litho-
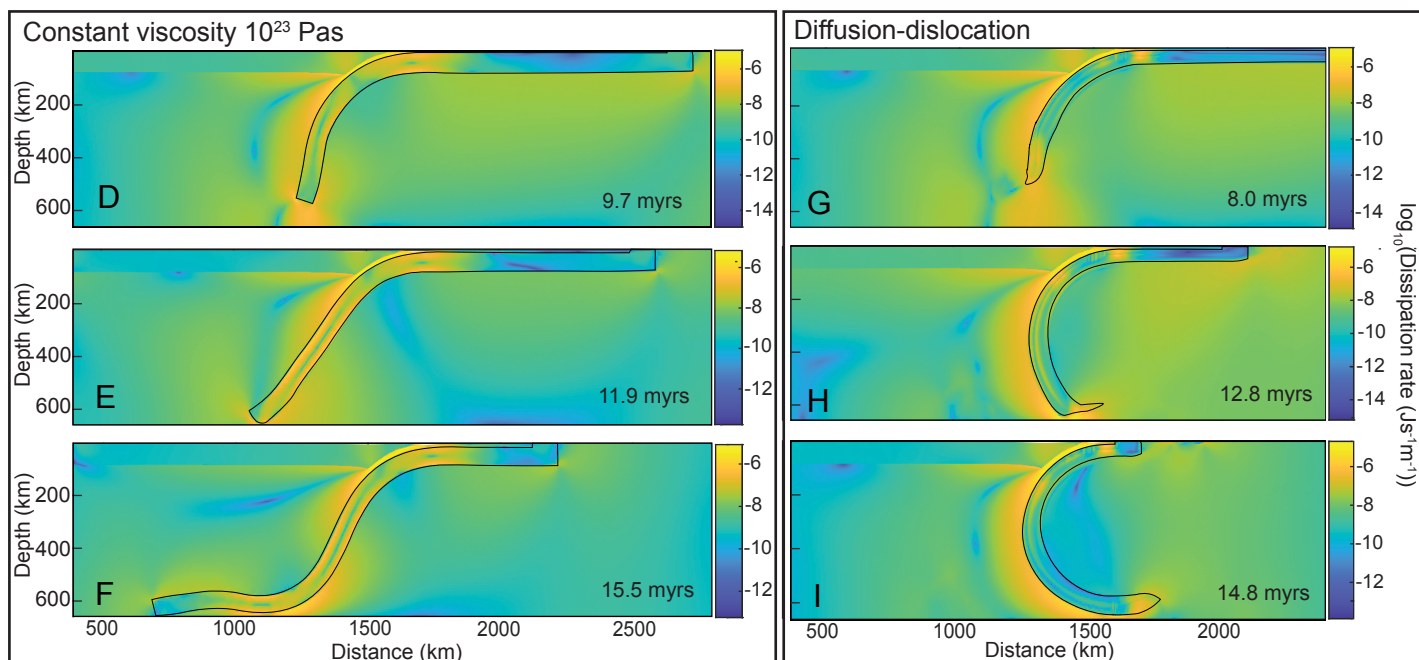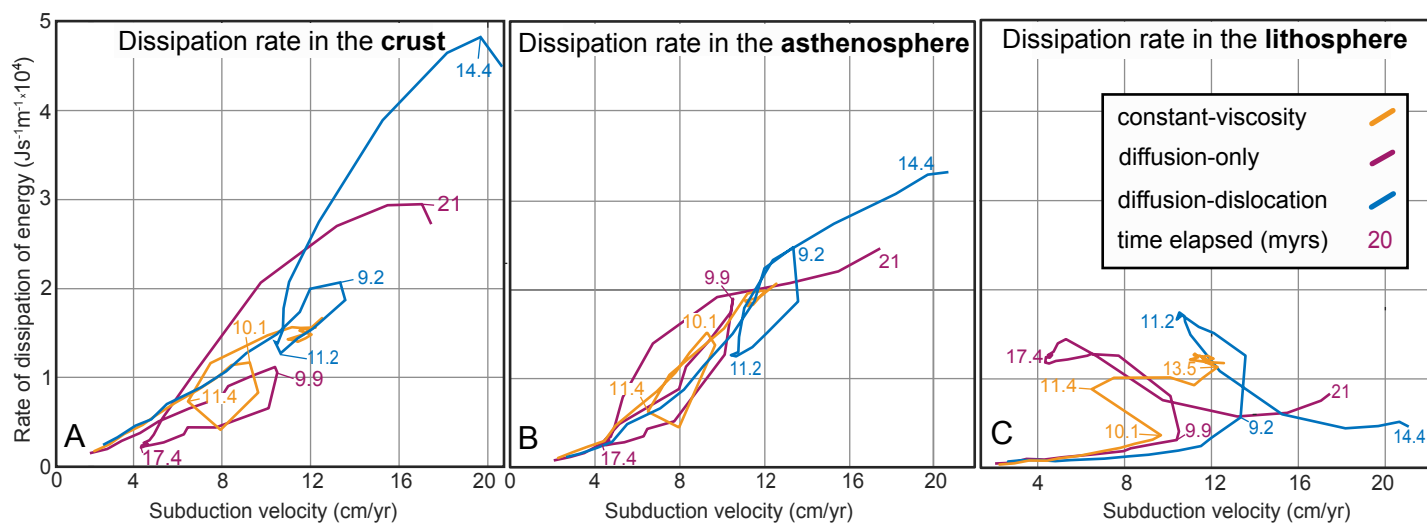
Figure 7. Dissipation rate in the crust (A), sub-lithospheric mantle (B), and slab mantle lithosphere (C) plotted against subduction velocity. The lines trace out the progression of each model over time, with selected points in time indicated in millions of years. Panels D-F show the distribution of energy dissipation in the reference model at 3 key snapshots. Panels G-I show distribution of energy dissipation for similar stages in the parallel diffusion-dislocation model. Plots are colored according to log_{10} of dissipation rate in J s^{-1}m^{-1}. In each panel, the portion of the slab that exceeds the viscosity of the asthenosphere is outlined in black.

spheric energy dissipation can be broken down into bending and stretching components. In free subduction models run by Capitanio et al. (2008), bending accounted for >80% of the total dissipation in strong slabs. Therefore, bending forces likely dominate lithospheric energy dissipation in our experiments. The rate of energy dissipation due to bending is:

$$F_{lith} = \frac{2}{3} * \frac{h^3}{R^3} * \eta * v_{sub}, \tag{5}$$

250

for lithosphere with a constant viscosity of η, a height of h, a radius of curvature, R, and a subduction velocity v_{sub} (Capitanio et al., 2008). The energy required to bend the lithosphere is therefore proportional to slab viscosity and the cube of slab thickness. This quantity, $\eta * h^3$, is the slab stiffness.

The diffusion-only slab has the highest stiffness of the creep-governed slabs, between $6 * 10^{39}$ and $4 * 10^{40}$ on the profile shown in Fig. 5 C. The minimum of this range is the stiffness calculated as a 40 km-thick region with a viscosity of 10^{26} Pas, and the maximum is the stiffness of a 75 km-thick slab with a viscosity of 10^{26} Pas. By the same logic, the dislocation and dislocation-diffusion controlled slabs have a stiffness between $4 * 10^{39}$ and $2 * 10^{40}$. In contrast, the constant-viscosity slab has a stiffness of $3.7 * 10^{37}$.

255

After the constant-viscosity slab develops a second bend at the bottom of the model (Fig. 7F), the overall resisting forces in the model reach an equilibrium with slab pull, resulting in a constant subduction velocity (Fig. 4A). This stage is also observed in the analogue models by Funiciello et al. (2008). In contrast, lithospheric dissipation in the creep-governed slabs increases dramatically in the middle of the run as the slab collides with the bottom of the model, and then decreases as the plate rolls under itself. The creep-governed slabs are able to maintain an approximately constant curvature after bending at the trench (Fig. 7I), resulting in a lower rate of energy dissipation at a given subduction velocity (Fig. 7C). Figure 6 shows a decrease in lithospheric dissipation rate, marked with vertical gray lines on the plots for creep-governed models, coinciding with a rapid increase in subduction velocity. The creep-governed models are not able to reach equilibrium between driving and resisting forces during the experiment, and subduction velocity continues to increase until the slab is consumed.

260

A key difference between the reference model and the creep-governed models is the rheology of the warm slab tip, which remains at 10^{23} Pas in the reference model and assimilates into the 10^{20} Pas mantle in the other models. Panels D and G of Figure 7 illustrate this contrast: at the time steps shown, the slab pull force is about $2 * 10^{13} N$ in both models, but the viscous portion of the constant-viscosity slab is longer than that of the diffusion-dislocation slab. The warm parts of the slab do not contribute to slab pull in any of the models. However, the strong slab tip in the reference model still provides resistance as the slab pushes through the mantle, increasing energy dissipation rate in the asthenosphere and the lithospheric mantle relative to the other models (Fig. 7B,C), despite the lower maximum viscosity in the core of the constant-viscosity slab. The extra drag around the slab tip likely contributes to the slightly lower subduction velocity of the constant-viscosity slab compared to the slabs with dislocation creep early in the model run (Fig. 4).

270

275

In order to differentiate between the effects of high stiffness and the more subtle effects of power-law creep, we simulated a slab with a constant viscosity of 10^{25} Pas. This slab has a stiffness of $5.1 * 10^{39}$, comparable to the stiffness of the creep-governed slabs, but lacks the more detailed viscosity structure imposed by the flow laws. The dissipation of energy over time

280 in this model is shown in the bottom panel of Figure 6. The model displays unrealistic behavior due to the free slip condition on the bottom boundary and the very high slab-to-mantle viscosity contrast. The tip of the slab becomes stuck pointing down at the bottom of the model and stalls subduction after 20 myrs, as shown in the inset. This geometry is similar to that observed by Ribe (2010) for slabs with viscosity contrasts exceeding 10^4. Before the slab makes contact with the bottom of the model, it subducts similarly to slabs in other models, but more slowly. This illustrates the degree to which the softened slab tips in

285 the creep-governed models increase plate velocity in the early stages of subduction and allow for the slab to roll under at the bottom boundary.

5 Discussion

5.1 Comparison to realistic slab rheology

Empirical evidence for the viscosity of subducting lithosphere is limited, but generally suggests weaker behavior than observed

290 in the creep-governed models presented here. Seismic strain rates from the Pacific plate at the Tonga-Kermadec trench (Holt, 1995) have only been matched in numerical models with maximum viscosities of 10^{24} Pas (Billen et al., 2003). This is two orders of magnitude lower than the highest viscosities in our models, which are already restricted to 10^{26} Pas by the maximum viscosity cap imposed by computational constraints. Additionally, most modern subducting slabs flatten out forward between 500 and 1200 km depth, or sink at a steep angle through the mantle transition zone (Goes et al., 2017). The only slab observed

295 to curl under itself, as our three creep-governed slabs do, is the Indian plate beneath the Himalayas (Goes et al., 2017), which, perhaps coincidentally, also has a very high subduction velocity. The slabs modeled here would likely have penetrated the mantle transition zone if the transition zone had been modeled with a viscosity contrast rather than a hard boundary (Billen, 2008). However, our slabs still appear to exhibit unusually stiff behavior despite moderate (<80 km) effective thicknesses.

Several studies have determined realistic slab-to-mantle viscosity ratios by comparing the results of numerical or analogue

300 models to observed slab geometries. Moresi and Gurnis (1996) match variations in the geoid near Western Pacific subduction zones using numerical models with slab-to-mantle viscosity ratios of 1-200, though larger values were not tested. Ribe (2010) matches observed slab curvatures with slab-to mantle viscosity ratios of 140-510, and Loiselet et al. (2009) obtain realistic slab curvatures with a ratio of 45. The analogue models of Schellart (2008) fit true slab geometries best with a viscosity ratio of 100-700. Our creep-governed models reach a ratio of 10^6 and resemble experiments with slabs deemed to have unrealistically

305 high viscosity contrasts in the above-mentioned studies. These studies suggest that, for a sub-lithospheric mantle viscosity of $10^{19} - 10^{20}$ Pas, slab viscosity should not exceed 10^{23} Pas. It is worth noting that all of these studies model slabs with a constant viscosity, and therefore do not preclude higher viscosity in small portions of a heterogeneous subducting plate.

Although viscosities modeled here appear unrepresentative of most real subduction zones, they do not stand out among numerical models of subduction in the literature. The slabs modeled by Gerya et al. (2021), Khabbaz Ghazian and Buiter

310 (2013), Tetreault and Buiter (2012), Tagawa et al. (2007), Billen and Hirth (2007), and Erdős et al. (2021), among others, reach 10^{25} or 10^{26} Pas in regions tens of kilometers thick. In shallow models, the lithosphere tends to curl fully underneath itself

(Khabbaz Ghazian and Buiter, 2013), as we observe in our creep-governed models. And in deeper models (Tagawa et al., 2007; Billen and Hirth, 2007), slabs often retain curvature through the mantle transition zone (Billen, 2008).

315 The high stiffness values observed in our experiments suggest that weakening mechanisms that we have not implemented play an important role in subduction zone deformation. Karato et al. (2001) and Kameyama et al. (1999) discuss the importance of Peierls creep to deformation in the cold interiors of subducting plates. Kameyama et al. (1999) show that, for grain sizes of approximately 1 mm, Peierls creep is active above stresses around 1000 MPa. In our models, creep-governed plates reach differential stresses above 1000 MPa in a region several tens of kilometers in thickness along most of their length, implying that Peierls creep should play an important role in their deformation.

320 Karato et al. (2001) proposed that grain size reduction due to mineral phase changes around 400 km depth could weaken the diffusion creep mechanism, helping to explain the discontinuity between observed slab strength and the predictions of diffusion and dislocation flow laws. Ĉížková et al. (2002) found that simulating a grain size reduction of several orders of magnitude weakens slabs significantly, but plays a smaller role tnhan a stress cap approximating Peierls creep.

Elsewhere, Gerya et al. (2021) argue that brittle failure at the trench may concentrate at periodic intervals along the length 325 of the slab. They show that, near the trench, below regions of extensive brittle deformation, increased stress may cause ductile damage that lowers grain sizes in the center of the slab. As the subducting plate moves deeper into the upper mantle, damaged areas maintain lower viscosities than undeformed areas, leading to sausage-like segmentation of the slab. The segmented slabs in their models move forward at the mantle transition zone despite reaching a viscosity of 10^{25} Pas in strong regions.

5.2 Implications for the interpretation of analogue models

330 It can be challenging to implement complex rheology in analogue models of subduction. Several analogue models have successfully incorporated temperature-dependent viscosity and a thermal gradient (Chemenda et al., 2000; Boutelier and Chemenda, 2003; Boutelier and Oncken, 2011), but the scaling of rheological properties in these experiments is less precise than what can be achieved through numerical modeling. In particular, as noted by Schellart and Strak (2016), in the models of Boutelier and Oncken (2011) and Boutelier and Chemenda (2003), the strength contrast between the lithosphere (a hydrocarbon mixture) 335 and the asthenosphere (liquid water) is several orders of magnitude too high. Faccenna et al. (1999), Funiciello et al. (2008), Husson et al. (2012), and Chen et al. (2015), among others, use viscous materials like silicone putty to achieve a more realistic viscosity contrast between the lithosphere and sub-lithospheric mantle, but neglect thermal effects. These models sometimes incorporate a layered structure to capture brittle behavior in the upper part of the plate, but typically use a constant-viscosity material for the viscous portion of the lithosphere.

340 Our numerical models illustrate the extent to which slabs with temperature- and pressure-dependent rheologies can be approximated by constant-viscosity analogue models. Before the slabs in our experiments reach the lower model boundary, subduction velocity and the rate of internal dissipation of energy follow similar patterns over time in all models—speeding up at an increasing rate before abruptly slowing down as the tip nears the mantle transition zone—regardless of the complexity of slab rheology (Fig. 6). Although the slabs with diffusion and dislocation creep curl under rather than sliding forward, it is

345   likely that a creep-governed slab with a lower stiffness would slide forward like our reference model. This indicates that the

qualitative behavior described by Funiciello et al. (2008) is not affected by increasing rheological complexity in the slab.

However, the entire length of the slab remains relatively stiff in analogue models and in our reference model, whereas

realistic temperature-dependent implementations cause the stiff portion of a slab to shorten as it is warmed by the surrounding

asthenosphere. The importance of this effective length change is illustrated by the difference in subduction velocity between the

350   experiment with a constant 10^{25} Pas slab and the two experiments with dislocation-controlled slabs. The dislocation-controlled

slabs subduct much more quickly than the constant 10^{25} Pas slab, reaching 660 km depth in approximately 11 myrs, in contrast

to 20 myrs. All three models have a slab stiffness around 10^{39}, but resistance in the slab tip and surrounding asthenosphere is

lower in the creep-governed models. This effect unrealistically reduces subduction velocity in our reference model and may

have a similar effect in constant-viscosity analogue models, although the density of the slab tip does not decrease with time in

355   these models as it does our reference model. Our results illustrate strong feedbacks between subduction velocity, slab pull, and

drag, which complicate quantitative inferences relating slab properties to subduction velocity from analogue models lacking

these feedbacks.

6   Conclusions

The rheological laws implemented in subducting slabs in this study produce a range of viscosity structures in the leading end of

360   the slab, which in turn affect subduction dynamics. The warm slab tip becomes soft like the asthenosphere in models following

creep flow laws and remains at higher viscosity in the (constant viscosity) reference model. This increases asthenospheric drag

and lithospheric bending resistance in the constant-viscosity model relative to the other models, which results in a lower rate

of subduction in the constant-viscosity model despite lower slab stiffness. These differences illustrate how the implementation

of more complex flow-controlled rheologies can impact the feedback between subduction velocity, slab pull, and resisting

365   forces relative to models with constant-viscosity lithosphere by shortening the effective length of the subducted slab. Most

analogue models of subduction resemble the constant-viscosity slab modeled here in that they do not implement temperature-

and pressure-dependant viscosity in the subducting lithosphere. Our results show that these models are likely to capture the

qualitative behavior of slabs with a more complex rheology, but may under-predict subduction velocity.

Models implementing only diffusion creep or dislocation creep, with brittle failure, predict unrealistically high viscosity

370   in the core of subducting lithosphere. Plasticity helps to weaken slabs at the surface, allowing them to bend. However, high

pressure prevents plasticity from lowering the effective viscosity of the lithosphere once it has subducted, resulting in very high

slab stiffness. The slab deforming by diffusion creep alone is particularly viscous. The dislocation creep mechanism is weaker

in all areas throughout the duration of our experiment, causing the dislocation-diffusion slab to behave nearly identically to the

dislocation-only slab.

375   Slab stiffness plays a critical role in subduction dynamics at all stages. Initially, as the slab tip sinks freely, higher slab

stiffness in the diffusion-only model compared to the models implementing dislocation creep increases energy dissipation rate

in the lithosphere (Fig. 7) and slows subduction (Fig. 4). Stiffness also controls whether the slab flattens out forward or curls

backwards after hitting the bottom of the model. This difference in slab geometry in turn results in dramatic differences in subduction velocity, slab dip, and trench rollback rate between the constant-viscosity slab and the stiffer, creep-governed slabs,

380 in part due to the limited domain of our models. In our creep-governed models, the viscosity maximum is reached in nearly half the thickness of the lithosphere. Therefore, it is important to consider the realistic implementation of weakening mechanisms such as Peierls creep or grain size reduction when designing numerical models of subduction.

7 Competing Interests

Susanne Buiter is an executive editor for Solid Earth. An independent editor supervised the peer-review process, and the authors
385 declare no other competing interests."

8 Acknowledgements

References

390   Arcay, D.: Dynamics of interplate domain in subduction zones: Influence of rheological parameters and subducting plate age, Solid Earth, 3, 467–488, https://doi.org/10.5194/se-3-467-2012, 2012.

Behr, W. M., Holt, A. F., Becker, T. W., and Faccenna, C.: The effects of plate interface rheology on subduction kinematics and dynamics, Geophysical Journal International, 230, 796–812, https://doi.org/10.1093/gji/ggac075, 2022.

Biemiller, J., Ellis, S., Mizera, M., Little, T., Wallace, L., and Lavier, L.: Tectonic inheritance following failed continental subduction: A

395   model for core complex formation in cold, strong lithosphere, Tectonics, 38, 1742–1763, https://doi.org/10.1029/2018TC005383, 2019.

Billen, M. I.: Modeling the dynamics of subducting slabs, Annual Review of Earth and Planetary Sciences, 36, 325–356, https://doi.org/10.1146/annurev.earth.36.031207.124129, 2008.

Billen, M. I. and Hirth, G.: Rheologic controls on slab dynamics, Geochemistry, Geophysics, Geosystems, 8, https://doi.org/10.1029/2007GC001597, 2007.

400   Billen, M. I., Gurnis, M., and Simons, M.: Multiscale dynamics of the Tonga-Kermadec subduction zone, Geophysical Journal International, 153, 359–388, 2003.

Boutelier, D. and Chemenda, A. and1 Burg, J.-P.: Subduction versus accretion of intra-oceanic volcanic arcs: Insight from thermo-mechanical analogue experiments, Earth and Planetary Science Letters, 212, 31–45, https://doi.org/10.1016/S0012-821X(03)00239-5, 2003.

Boutelier, D. and Oncken, O.: 3-D thermo-mechanical laboratory modeling of plate-tectonics: Modeling scheme, technique and first experi-

405   ments, Solid Earth, 2, 31–51, https://doi.org/10.5194/se-2-35-2011, 2011.

Buiter, S. J. H. and Ellis, S. M.: SULEC: Benchmarking a new ALE finite-element code, Geophysical Research Abstracts, EGU General Assembly, 14, 2012.

Capitanio, F., Morra, G., and Goes, S.: Dynamic models of downgoing plate-buoyancy driven subduction: Subduction motions and energy dissipation, Earth and Planetary Science Letters, 262, 284–297, https://doi.org/10.1016/j.epsl.2007.07.039, 2008.

410   Chemenda, A. I., Burg, J. P., and Mattauer, M.: Evolutionary model of the Himalaya–Tibet system: geopoem: based on new modelling, geological and geophysical data, Earth and Planetary Science Letters, 174, 397–409, https://doi.org/10.1016/S0012-821X(99)00277-0, 2000.

Chen, Z., Schellart, W., and Duarte, J.: Overriding plate deformation and variability of fore-arc deformation during subduction: insight from geodynamic models and application to the Calabria subduction zone, Geochem. Geophys. Geosyst., 16, 3697–3715,

415   https://doi.org/10.1002/2015GC005958, 2015.

Chopra, P. and Paterson, M.: The experimental deformation of dunite, Tectonophysics, 78, 453–473, 1981.

Čížková, H., van Hunen, J., van den Berg, A. P., and Vlaar, N. J.: The influence of rheological weakening and yield stress on the interaction of slabs with the 670 km discontinuity, Earth and Planetary Science Letters, 199, 447–457, 2002.

Crameri, F.: Scientific colour maps, Zenodo, https://doi.org/10.5281/zenodo.1243862, 2018.

420   Culling, W.: Analytical theory of erosion, The Journal of Geology, 68, 336–344, 1960.

Davies, J. H.: Simple analytical model for subduction zone structure, Geophysical Journal International, 139, 823–828, 1999.

DiGiuseppe, E., van Hunen, F., Funiciello, F., Faccenna, C., and Giardini, D.: Slab stiffness control of trench motion: Insights from numerical models, Geochemistry Geophysics and Geosystems, 9, https://doi.org/10.1029/2007GC001776, 2008.

Erdős, Z., Huismans, R. S., Faccenna, C., and Wolf, S. G.: The role of subduction interface and upper plate strength on back-arc extension:

425   Application to Mediterranean back-arc basins., Tectonics, 40, https://doi.org/10.1029/2021TC006795, 2021.

Faccenna, C., Giardini, D., Davy, P., and Argentieri, A.: Initiation of subduction at Atlantic-type margins; insights from laboratory experiments., Journal of Geophysical Research, 104, 2749–2766, https://doi.org/10.1029/1998JB900072, 1999.

Funiciello, F., Faccenna, C., Giardini, D., and Regenauer-Lieb, K.: Dynamics of retreating slabs: 2. Insights from three-dimensional laboratory experiments, Journal of Geophysical Research, 108, https://doi.org/10.1029/2001JB000896, 2008.

430   Gerya, T. V., Bercovici, D., and Becker, T. W.: Dynamic slab segmentation due to the brittle-ductile damage in the outer rise, Nature, 599, 245–250, https://doi.org/10.1038/s41586-021-03937-x, 2021.

Goes, S., Agrusta, R., van Hunen, J., and Garel, F.: Subduction-transition zone interaction: A review, Geosphere, 13, https://doi.org/10.1130/GES01476.1., 2017.

Guyot, P. and Dorn, J. E.: A critical review of the Peierls mechanism, Canadian Journal of Physics, 45, https://doi.org/10.1139/p67-073, 435   1967.

Hager, B. H.: Subducted slabs and the geoid: Constraints on mantle rheology and flow, Journal of Geophysical Research, 89, 6003–6015, https://doi.org/10.1029/JB089iB07p06003, 1984.

Heuret, A., F. F. F.-C. . L. S.: PLate kinematics, slab shape and back-arc stress: A comparison between laboratory models and current subduction zones, Earth and Planetary Science Letters, 256, 473–483, https://doi.org/10.1016/j.epsl.2007.02.004, 2007.

440   Hirth, G. and Kohlstedt, D.: Rheology of the upper mantle and the mantle wedge: A view from the experimentalists, Geophysical Monograph, 138, 83–105, https://doi.org/10.1029/138GM06, 2003.

Holt, W. E.: Flow fields within the Tonga Slab determined from the moment tensors of deep earthquakes, Geophysical Research Letters, 22, 989–992, https://doi.org/10.1029/95GL00786, 1995.

Hummel, N. and Erdős, Z.: The influence of slab rheology on numerical models of subduction (code), 445   https://doi.org/10.5281/zenodo.8161409, 2023.

Husson, L., Guillaume, B., Funiciello, F., Faccenna, C., and Royden, L.: Unraveling topography around subduction zones from laboratory models, Tectonophysics, 526, 5–15, 2012.

Kameyama, M., Yuen, D. A., and Karato, S. I.: Thermal-mechanical effects of low-temperature plasticity (the Peierls mechanism) on the deformation of a viscoelastic shear zone, Earth and Planetary Science Letters, 168, 159–172, 1999.

450   Karato, S. and Wu, P.: Rheology of the upper mantle: A synthesis, Science, 260, 771–778, https://doi.org/10.1126/science.260.5109.77, 1993.

Karato, S., Riedel, M. R., and Yuen, D. A.: Rheological structure and deformation of subducted slabs in the mantle transition zone: implications for mantle circulation and deep earthquakes, Physics of Earth and Planetary Interiors, 3994, 2001.

Kaus, B. J. P. and Becker, T. W.: A numerical study on the effects of surface boundary conditions and rheology on slab dynamics, Bollettino di Geofisica Teorica ed Applicata, 49, 177–182, 2008.

455   Khabbaz Ghazian, R. and Buiter, S. J. H.: A numerical investigation of continental collision styles, Geophysical Journal International, 193, ł133–1152, https://doi.org/10.1093/gji/ggt068, 2013.

Kirby, S.: Rheology of the lithosphere, Reviews of Geophysics, 21, 1458–1487, https://doi.org/10.1029/RG021i006p01458, 1983.

Loiselet, C., Husson, L., and Braun, J.: From longitudinal slab curvature to slab rheology, Geology, 37, 747–750, https://doi.org/10.1130/G30052A.1, 2009.

460   Moresi, L. and Gurnis, M.: Constraints on the lateral strength of slabs from three-dimensional dynamic flow models, Earth and Planetary Science Letters, 138, 15–28, 1996.

Pysklywec, R. and Beaumont, C.: Intraplate tectonics: feedback between radioactive thermal weakening and crustal deformation driven by mantle lithosphere instabilities, Earth and Planetary Science Letters, 221, 275–292, 2004.

Quinquis, M. E. T. and Buiter, S. J. H.: Testing the effects of basic numerical implementations of water migration on models of subduction dynamics, Solid Earth, 5, 537–555, https://doi.org/10.5194/se-5-537-2014, 2014.

Quinquis, M. E. T., Buiter, S. J. H., and Ellis, S.: The role of boundary conditions in numerical models of subduction zone dynamics, Tectonophysics, 497, 57–70, https://doi.org/10.1016/j.tecto.2010.11.001, 2011.

Ranalli, G.: Rheology of the Earth, Springer Book Archive, 2 edn.

Reiner, M.: The Deborah number, Physics Today, 17, 62, https://doi.org/10.1063/1.3051374, 1964.

Ribe, N.: Bending mechanics and mode selection in free subduction: a thin-sheet analysis, Geophysical Journal International, 180, 559–576, https://doi.org/10.1111/j.1365-246X.2009.04460.x., 2010.

Schellart, W.: Kinematics and flow patterns in deep mantle and upper mantle subduction models: influence of the mantle depth and slab to mantle viscosity ratio, Geochemistry Geophysics and Geosystems, 9, https://doi.org/10.1029/2007gc001656, 2008.

Schellart, W. P. and Strak, V.: A review of analogue modelling of geodynamic processes: Approaches, scaling, materials and quantification, with an application to subduction experiments, Journal of Geodynamics, 100, 7–32, https://doi.org/10.1016/j.jog.2016.03.009, 2016.

Schenk, O. and Gartner, K.: Solving unsymmetric sparse systems of linear equations with PARDISO, Journal Future Generation Computer Systems, 20, 475–487, 2004.

Schmeling, H., Babeyko, A. Y., Faccenna, C., Funiciello, F., Gerya, T., Golabek, G. J., Grigull, S., Kaus, B. J. P., Morra, G., and van Hunen, J.: A benchmark comparison of spontaneous subduction models–Towards a free surface, Physics of the Earth and Planetary Interiors, https://doi.org/10.1016/j.pepi.2008.06.028, 2008.

Stegman, D. R., Farrington, R., Capitanio, F. A., and Schellart, W. P.: A regime diagram for subduction styles from 3-D numerical models of free subduction, Tectonophysics, 483, 29–45, https://doi.org/10.1016/j.tecto.2009.08.041, 2010.

Tagawa, M., Nakakuki, T., Kameyama, M., and Tajima, F.: The role of history-dependent rheology in plate boundary lubrication for generating one-sided subduction, Pure and applied geophysics, 164, 879–907, https://doi.org/10.1007/s00024-007-0197-4, 2007.

Tetreault, J. L. and Buiter, S. J. H.: Geodynamic models of terrane accretion: Testing the fate of island arcs, oceanic plateaus, and continental fragments in subduction zones, Journal of Geophysical Research, 117, https://doi.org/10.1029/2012JB009316, 2012.

Torii, Y. and Yoshioka, S.: Physical conditions producing slab stagnation: Constraints of the Clapeyron slope, mantle viscosity, trench retreat, and dip angles, Tectonophysics, 445, 200–209, https://doi.org/10.1016/j.tecto.2007.08.003, 2007.

Turcotte, D. L. and Schubert, G.: Geodynamics, Cambridge University Press, New York, 2014.

van den Berg, A., van Keken, P., and Yuen, D.: The effects of a composite non-Newtonian and Newtonian rheology on mantle convection, Geophys. J. Int., 115, 62–78, 1993.

van Hunen, J., Zhong, S., Shapiro, N. M., and Ritzwoller, M. H.: New evidence for dislocation creep from 3-D geodynamic modelling of the Pacific upper mantle structure, Earth and Planetary Science Letters, 238, 146–155, https://doi.org/10.1016/j.epsl.2005.07.006, 2005.

Wilks, K. and Carter, N.: Rheology of some continental lower crustal rocks, Tectonophysics, 182, 57–77, 1990.

Video supplement. Animations of the experiments can be found at https://doi.org/10.5446/62583.